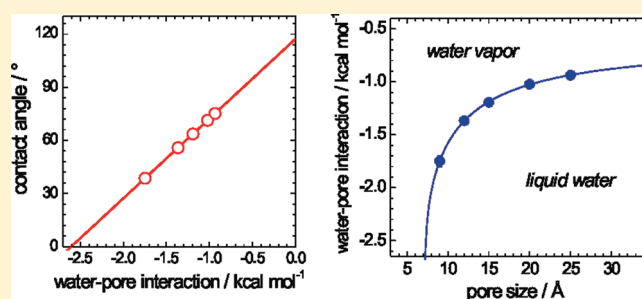


Effect of Pore Size on the Condensation/Evaporation Transition of Confined Water in Equilibrium with Saturated Bulk Water

Ivan Brovchenko* and Alla Oleinikova*

Physical Chemistry, Dortmund University of Technology, Otto-Hahn-Strasse 6, Dortmund, D-44227, Germany

ABSTRACT: The effect of pore size on the condensation/evaporation transition of confined water upon varying the strength of the water–surface interaction is studied under conditions of equilibrium with saturated bulk. Monte Carlo simulations in the grand canonical ensemble were used to determine water density in spherical pores of radius $R_p = 9, 12, 15, 20,$ and 25 \AA in the temperature range from $T = 270 \text{ K}$ to the bulk critical temperature. The critical values of the well depth of the water–surface interaction potential, which mark the limits of the metastability of vapor and liquid phases in pores (U_0^{cond} and U_0^{evap} , respectively), were determined. U_0^{cond} strongly depends on temperature, practically does not depend on the pore size, and corresponds to some particular density of water vapor near a surface. In contrast, U_0^{evap} only slightly depends on temperature, depends strongly on pore size, and corresponds to the density in the pore interior by about 2% below the bulk value. The critical water–pore interaction U_0^c , which separates regimes of capillary condensation and capillary evaporation, is found to be changed from -1.75 to -0.94 kcal/mol when the pore radius R_p increases from 9 to 25 \AA . The size dependence of U_0^c is attributed to the change of the contact angle due to the line tension effect. Extrapolation of the dependence $U_0^c(R_p)$ to the flat surface gives the critical value $U_0^c(\infty) \approx -0.61 \text{ kcal/mol}$.



1. INTRODUCTION

The condensation/evaporation transition of water in porous materials has been studied extensively experimentally, theoretically, and by simulations as it is important in various technological applications. These studies were focused mainly on the porous materials, whose interaction with water is constant. During recent years, responsive surfaces with varying wettability have been developed. The contact angle θ of liquid water on such surfaces can be varied in a wide range: from values close to 0° (strongly hydrophilic surface) to values close to 180° (strongly hydrophobic surface). This can be done reversibly by varying temperature, applying electric field, light irradiation, adsorption/desorption of macromolecules, etc.^{1–5} Synthesis of porous materials with thermo-responsive surfaces has been already reported.^{6–8} It is natural to expect that the adsorptive behavior of responsive porous materials can be very complex. This new class of porous materials can be promising in technological applications, where adsorption/desorption of water is used, as their adsorptive properties can be purposefully varied by some external impact.

Responsive porous materials should be especially useful in applications related to storage of heat and cold.^{9,10} Nowadays, there is an urgent need in developing highly efficient heat-storage devices for saving energy in various applications: from air conditioning to power plants. Heat can be stored by evaporation of liquid water from porous material and released later by condensation of external water vapor in dry porous material. The variation of the water–surface interaction allows control of the condensation/evaporation transition in pores. A key

parameter, which should be known for efficient optimization of such porous materials for practical applications, is the critical water–surface interaction, which separates regimes of capillary condensation and capillary evaporation at various thermodynamic states of the external (bulk) water vapor.

Simulation studies of the condensation/evaporation transition upon varying the strength of the water–pore interaction are rare.^{10–13} Recently, the temperature dependence of the critical value U_0^c for water in a spherical pore of radius $R_p = 12 \text{ \AA}$ was studied in a wide temperature range (up to the bulk critical temperature) using the grand canonical ensemble and varying the well depth U_0 of the water–surface potential of the pore under conditions of equilibrium with the saturated bulk water.¹⁰ The obtained critical value $U_0^c \approx -1.35 \pm 0.03 \text{ kcal/mol}$, which separates regimes of capillary condensation and capillary evaporation, has been found practically insensitive to temperature. Besides, the domains of the metastable liquid and vapor phases in the $T - U_0$ coordinates have been determined. The stability limits for vapor and liquid phases in the pore at low temperatures were found at $U_0 \approx -2.8$ and -1.2 kcal/mol , respectively, and they merge at the pore hysteresis critical temperature at about 415 K .

The phase diagram of confined fluid strongly depends on the pore size and shape.^{14–19} It is not clear to what extent the critical value U_0^c , which separates the regimes of capillary condensation

Received: December 19, 2010

Revised: May 9, 2011

Published: August 03, 2011

and capillary evaporation, is universal. In accordance with the Kelvin equation,²⁰ the condensation/evaporation transition in a pore in equilibrium with the saturated bulk occurs when the fluid–surface interaction is equal to the critical value, which provides a contact angle $\theta = 90^\circ$. Therefore, the value U_0^c is expected to be universal when the validity of the Kelvin equation and the value of the contact angle are not affected by the small system size. The dependence of the value U_0^c on pore size can originate from the corrections to the Kelvin equation as well as from the corrections to the contact angle, which gain more importance with decreasing pore size. It is not clear in advance, which corrections are the most important for the problem considered.

Spherical-like cages and cylindrical-like channels are the key structural elements of many porous materials. MCM-41-type materials consist of a hexagonal arrangement of cylindrical pores, whose length can exceed their diameter by the order of the magnitude.²¹ SBA-16, KIT-5, and FDU-12 porous silica materials consist of a three-dimensional arrangement of almost spherical cavities connected through narrow necks of molecular dimensions.^{22,23} The structure of other porous materials (zeolites, Vycor glasses, silica gels, etc.) is composed of a network of interconnected channels and cages. Therefore, it is reasonable to start the analysis of the size effect on the value U_0^c for fluids in spherical and cylindrical pores. In the present paper, we study the effect of pore size on the liquid–vapor transition of water in spherical pores. This simple pore geometry has been actively used in the theoretical and simulation studies of confined fluids.^{11,24–29} By varying the water–surface interaction, we study adsorption and desorption of water in pores at various temperatures in equilibrium with saturated bulk water and determine stability limits for confined liquid and vapor. Above the hysteresis pore critical temperatures, the water–surface interactions U_0^c corresponding to the condensation/evaporation transition are estimated for the pores of various sizes. Physical mechanisms, which can be responsible for the dependence of U_0^c on pore radius, are analyzed.

METHODS

Model Pores. The pore was modeled as a spherical cavity in a solid material composed of monodisperse spherical particles. The potential energy of the interaction of a water molecule with a solid material U_{ws} was represented as a sum of the LJ (6–12) potentials between water oxygen and i th particle of diameter σ separated by distance x_i

$$U_{ws} = \sum_i 4\epsilon \left[\left(\frac{\sigma}{x_i} \right)^{12} - \left(\frac{\sigma}{x_i} \right)^6 \right] \quad (1)$$

In continuous approximation and upon homogeneous distribution of substrate particles, the dependence of U_{ws} on the distance r between water oxygen and the surface of a spherical cavity can be obtained by integration within some spherical shell of a solid material. In the present study, the potential $U_{ws}(r)$ in the spherical pores was obtained by numerical integration of the potentials U_{ws} given by eq 1 with $\sigma = 3.5$ Å within the spherical shell of width W of a solid material forming the pore walls. For integration, the spherical layer was divided into subshells of thickness 0.0075 Å and the integration step for the angle was 0.14° . It was found that the obtained potential $U_{ws}(r)$ practically does not depend (within 0.2%) on the thickness W of the pore walls at $W \geq 20$ Å and does not change upon further decreasing the integration steps.¹⁰

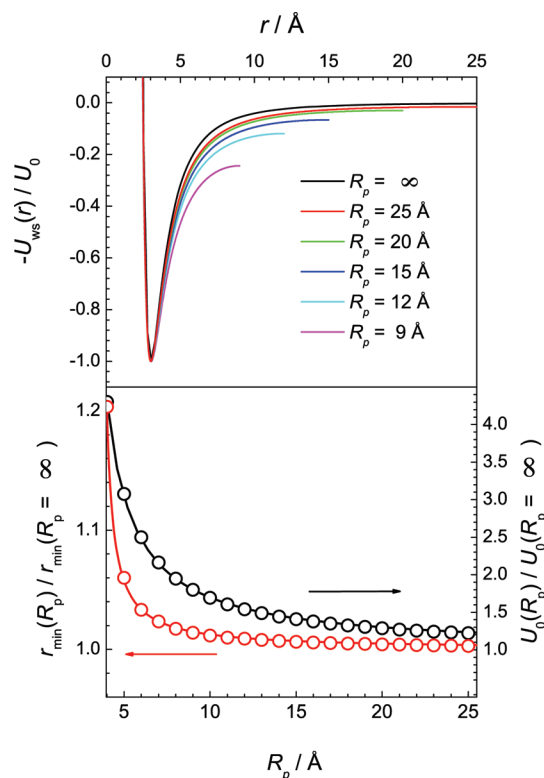


Figure 1. (Top) Potential energy U_{ws} of a water molecule in spherical pores of various radii R_p formed in the same material normalized by its minimal value U_0 as a function of the distance r between water oxygen and the pore surface. The pore radii are indicated on the figure. (Bottom) Ratio of the well-depth U_0 of water–surface potentials in a spherical pore to its value near the planar surface $U_0(R_p = \infty)$ as a function of pore radius R_p (black symbols); the location r_{min} of the potential well relative to the pore surface as a function of the pore radius R_p (red symbols). The lines are the fits to the eq 2.

We calculated $U_{ws}(r)$ in pores of various radii with wall thickness $W = 30$ Å. The potential $U_{ws}(r)$ normalized by its well depth U_0 is shown in the upper panel of Figure 1 for the pores used in the present studies. In the limit $R_p \rightarrow \infty$ (planar surface), the water–surface interaction potential $U_{ws}(r)$ is a LJ (3–9) potential (see ref 10 for more details). The attractive tail of $U_{ws}(r)$ shows a slower decay upon decreasing pore size. The well depth U_0 of the potential $U_{ws}(r)$ generated in the spherical pore by the same solid material becomes deeper with decreasing pore size. The dependence of the ratio $U_0(R_p)/U_0(R_p = \infty)$ on the pore radius R_p is shown in the lower panel of Figure 1. In the large pore with $R_p = 350$ Å, $|U_0|$ is by less than 1% exceeds $|U_0|$ near planar surface. The deepest potential well, which is by a factor of about 7 exceeds $|U_0|$ near planar surface, is observed in the pore with $R_p = 3.95$ Å, when two minima of U_0 seen in larger pores along the pore diameter merge together in the pore center. The location r_{min} of a potential well moves away from the surface with decreasing pore size (see lower panel in Figure 1). In the pores with $R_p \geq 9$ Å, r_{min} deviates from the value near the planar surface (3.0 Å) by less than 0.01 Å. The dependences $U_0(R_p)/U_0(R_p = \infty)$ and $r_{min}(R_p)/r_{min}(R_p = \infty)$ on R_p for $R_p \geq 4.0$ Å can be well fitted by the empirical equation

$$A(R_p)/A(R_p = \infty) = 1 + \frac{B}{(R_p - C)} \quad (2)$$

where A stands for U_0 or r_{\min} . The fitting curves with $B = 2.4 \text{ \AA}$ and $C = 5.3 \text{ \AA}$ for the dependence $U_0(R_p)/U_0(R_p = \infty)$ and with $B = 3.6 \text{ \AA}$ and $C = 0.8 \text{ \AA}$ for the dependence $r_{\min}(R_p)/r_{\min}(R_p = \infty)$ are shown by lines in the lower panel of Figure 1.

Thus, in the porous material formed by the cavities of various sizes in some homogeneous solid material, the water–surface interaction strongly depends on the cavity size, especially in small pores (Figure 1). In many real porous materials, the pore surface differs essentially from the bulk solid and the water–pore interaction is determined by the short-range water–surface interaction (such as hydrogen bonds). In such pores, the water–pore interaction can be expected to be not dependent on the pore size. Therefore, in the present paper we consider the case when the well depth U_0 of the water–pore interaction does not depend on the pore size.

Simulations of the Condensation/Evaporation Transition.

The TIP4P model with a spherical cutoff at 8.5 \AA was used for water.³⁰ Water in spherical pores of radii $R_p = 9, 12, 15, 20$, and 25 \AA was simulated in the temperature range from 270 K to the liquid–vapor critical temperature of TIP4P water $T_c^b \approx 580 \text{ K}$. For three smaller pores, the simulations have been performed with a temperature step of 10 K (32 temperatures for each pore). For two larger pores with $R_p = 20$ and 25 \AA , the simulations have been performed at 8 and 6 temperatures, respectively. The number of water molecules in the liquid phase of confined water at low temperatures increased from ~ 60 in the smallest pore to ~ 2000 in the largest pore studied. Monte Carlo (MC) simulations of water in model spherical pores were performed in the grand canonical ensemble³¹ with the value of the chemical potential fixed at the value of the saturated bulk water at the same temperature. The chemical potential of bulk TIP4P water along the liquid–vapor coexistence curve has been obtained in our recent paper.¹⁰ The type of subsequent MC step has been chosen randomly in order to provide 20% of the displacement/rotation steps, 40% of deletion steps, and 40% of insertion steps. Up to 2×10^9 MC steps have been performed for each state point, and system properties have been analyzed every 10^4 th MC step for smaller pores ($R_p \leq 15 \text{ \AA}$) and every 5×10^4 th MC step for larger pores ($R_p \geq 20 \text{ \AA}$).

At each temperature, simulations were performed at various well depths U_0 of the water–surface potential. U_0 was varied from -0.5 to -8.3 kcal/mol , which corresponds to the variation of the pore surface from strongly hydrophobic to strongly hydrophilic. U_0 was varied with a step of about 1.0 kcal/mol far from the condensation/evaporation transition, whereas the step was decreased to about 0.03 kcal/mol in the regions of the strong changes of the pore water density upon varying U_0 . From 14 to 28 values of the well depths U_0 were used at each temperature. In total, about 2000 state points have been studied. Simulations have been started from the empty pore for adsorption branch of the isotherm $\rho(U_0)$ and from the pore filled with liquid water for its desorption branch. The average density of confined water ρ was calculated, assuming that water occupies the volume of a sphere with radius $R_p^* = R_p - 1.25 \text{ \AA}$.³² For more details of the simulations in the grand canonical ensemble, see ref 10.

RESULTS

The density of confined water at $T = 300 \text{ K}$ in pores of various sizes is shown in Figure 2 as a function of U_0 . At this temperature, the phase state of confined water (liquid or vapor) depends on

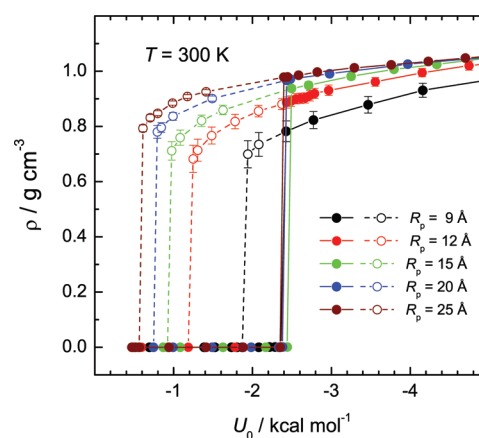


Figure 2. Density of water in pores of various sizes in equilibrium with the saturated bulk at $T = 300 \text{ K}$ as a function of the strength U_0 of the water–surface interaction. Solid and open symbols represent simulation runs when the initial state of fluid in the pore was vapor (adsorption) and liquid (desorption), respectively. Error bars represent the standard deviations of ρ .

the initial state in a particular simulation run. As a result, the isotherms $\rho(U_0)$ show a hysteresis loop within some interval ΔU_0 , which increases with increasing pore size. Upon strengthening the water–surface interaction, water remains in a vapor phase until some value U_0^{cond} , which is a limit of stability for vapor. This value was calculated as an average of the largest $|U_0|$ value when vapor survives in a pore during the simulation run and the lowest $|U_0|$ value when spontaneous condensation occurs. In a similar way, a limit of stability for liquid U_0^{evap} was defined from the desorption branch of the isotherms $\rho(U_0)$ (see ref 10 for more details). The accuracy in the estimation of U_0^{cond} and U_0^{evap} is determined by the step in U_0 used in the vicinity of the spontaneous condensation and evaporation, respectively. This step was about 0.07 and 0.05 kcal/mol for the smallest and largest pore studied, respectively.

The stability limits U_0^{cond} and U_0^{evap} for water vapor and liquid in all studied pores at various temperatures are shown in Figure 3 by closed and open symbols, respectively. U_0^{cond} varies strongly with temperature, and it is almost independent of pore size. This means that the spontaneous condensation upon heating and (or) strengthening the water–surface interaction occurs almost simultaneously in pores of various sizes which have the same water–surface interaction potential. The value of U_0^{cond} ranges from about -2.7 kcal/mol at low temperatures to about -0.7 kcal/mol on approaching the bulk critical temperature in large pores. In contrast, U_0^{evap} shows weak temperature dependence and decreases strongly upon pore narrowing. Therefore, evaporation of liquid water from pores upon weakening water–surface interaction occurs within a rather wide range of U_0 of about 1.2 kcal/mol for the considered range of pore sizes. Due to the weak temperature dependence of U_0^{evap} , spontaneous evaporation upon heating is only possible within a rather narrow range of U_0 , and this range depends strongly on pore size.

Practically simultaneous occurrence of the spontaneous condensation of metastable vapor upon increasing temperature and/or strengthening the water–surface interaction in pores of various sizes (Figure 3) can indicate that the phenomenon of spontaneous condensation is driven by the local properties of water near a surface. To test this option, we calculated the water vapor density profiles $\rho(r)$ at $T = 300 \text{ K}$ in the pores with values

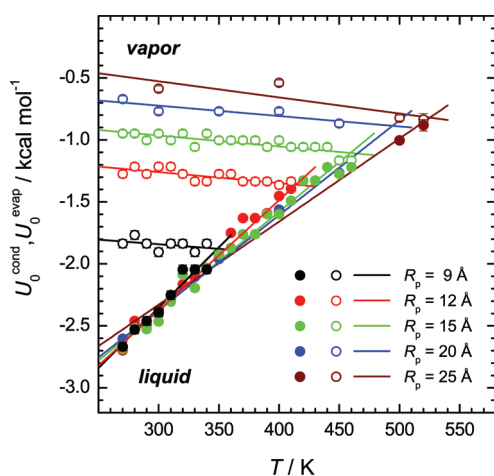


Figure 3. Temperature dependence of the stability limits for vapor (U_0^{cond} , close circles) and liquid (U_0^{evap} , open circles) phases of water in pores of various sizes. Error bars correspond to the step in U_0 used in the simulations. The linear fits are shown by lines.

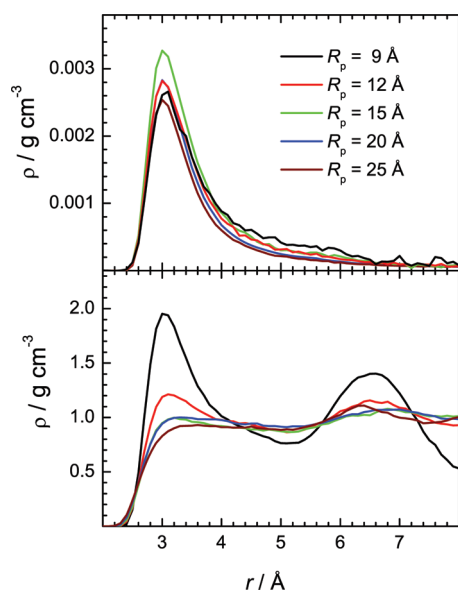


Figure 4. Density profiles of water in various pores close to the stability limits for vapor (top) and liquid (bottom) at $T = 300$ K.

of U_0 closest to the stability limits for vapor U_0^{cond} . As can be seen from Figure 4(top), the density profiles are similar in all pores and do not show dependence on the pore radius. To calculate the density ρ_1 of water in the surface layer, we considered water molecules as belonging to this layer if the distances between their oxygens and pore surface did not exceed 4.5 Å. The values ρ_1 obtained from the density profiles are given in Table 1. They do not correlate with the pore radius but clearly correlate with the value U_0 used in simulations, which is minimal for the pore with $R_p = 15$ Å and maximal for the pore with $R_p = 25$ Å. In contrast, the density of water in the pore interior ρ_{in} (water apart of the surface layer) decreases monotonically with increasing pore size and becomes about 4 times lower when the pore radius increases from 9 to 25 Å. Therefore, we conclude that the stability limit for vapor is determined by the vapor density in the surface layer. At $T = 300$ K, spontaneous condensation of water vapor in pores

Table 1. Values of the Water Density in the Surface Layer ρ_1 and in the Pore Interior ρ_{in} Close to the Stability Limits for Vapor and Liquid in Pores with Radius R_p

R_p (Å)	U_0 (kcal/mol)	ρ_1 (g/cm ³)	ρ_{in} (g/cm ³)
close to the stability limit for vapor (U_0^{cond})			
9	−2.39	7.2×10^{-4}	3.3×10^{-4}
12	−2.40	7.8×10^{-4}	1.9×10^{-4}
15	−2.47	9.2×10^{-4}	1.6×10^{-4}
20	−2.41	7.9×10^{-4}	1.0×10^{-4}
25	−2.37	7.1×10^{-4}	8.1×10^{-5}
close to the stability limit for liquid (U_0^{evap})			
9	−1.91	0.64	0.92
12	−1.22	0.53	0.96
15	−0.95	0.49	0.96
20	−0.77	0.52	0.98
25	−0.59	0.50	0.98

occurs when the density of water vapor in the surface layer achieves $\sim 8 \times 10^{-4}$ g/cm³. This value by about 70 times exceeds the saturated vapor density of bulk TIP4P water at the same temperature ($\sim 1.2 \times 10^{-5}$ g/cm³).³³

The density profiles of liquid water at $T = 300$ K in the pores with values of U_0 closest to the stability limits for liquid U_0^{evap} are shown in the lower panel of Figure 4. The density of liquid water in the surface layer strongly decreases with increasing pore size: ρ_1 in the smallest pore is about 22% larger than ρ_1 in the largest pore (Table 1). In contrast, the density in the pore interior increases by just 7% with increasing pore size. We can assume that spontaneous evaporation of liquid in pores starts from the pore interior as it is determined by the density of liquid water in this region. At $T = 300$ K, liquid in the interior of large pores becomes unstable when its density decreases to ~ 0.98 g/cm³, which is only by 0.02 g/cm³ lower than the density of the saturated bulk liquid water. This agrees with the results of the recent experiments on the cavitation of bulk water at negative pressures, where it starts at $\rho \approx 0.985$ g/cm³ at $T = 300$ K.³⁴

The width of a hysteresis loop in terms of the water–surface potential, $\Delta U_0 = U_0^{\text{evap}} - U_0^{\text{cond}}$, shrinks upon heating and disappears at the hysteresis pore critical temperature T_c^h . The values U_0^{evap} and U_0^{cond} change roughly linearly upon heating (see linear fits shown by straight lines in Figure 3). For three smaller pores, where the temperature step in simulations was 10° , the hysteresis critical temperature was defined as an average value between the highest temperature, where the hysteresis is observed, and the lowest temperature, where adsorption and desorption branches of the isotherm $\rho(U_0)$ coincide. For two pores with $R_p \geq 20$ Å, where the temperature step was larger, T_c^h was estimated as a crossing point of the linear fits of the dependences $U_0^{\text{evap}}(T)$ and $U_0^{\text{cond}}(T)$, where $\Delta U_0 = 0$. The estimated values of T_c^h for all pores are shown in Figure 5 as a function of the pore radius R_p .

Theory reveals that the shift $\Delta T_c = T_c^b - T_c^p$ of the liquid–vapor critical temperature in pore T_c^p with respect to the bulk critical temperature T_c^b depends on the pore width H as $\sim H^{-1}$ in small pores and as $\sim H^{1/0.63}$ in large pores, when T_c^p approaches T_c^b with increasing pore size.^{35,36} The dependences $\Delta T_c \approx H^{-1}$ have been observed in both experimental and simulation studies of fluids in pores (see ref 17 and references therein). Rather similar size dependences have been observed also for the hysteresis pore critical temperature T_c^h .^{37,38} We fitted the dependence

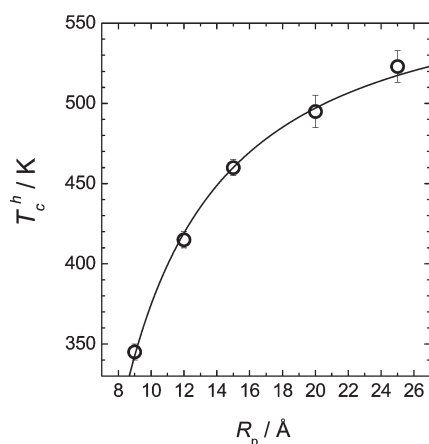


Figure 5. Hysteresis pore critical temperature T_c^h as a function of the pore radius R_p (symbols). Error bars correspond to the temperature step used in simulations. The fit of the dependence $T_c^h(R_p)$ to eq 3 is shown by the line.

$T_c^h(R_p)$ shown in Figure 5 to the equation

$$T_c^h = T_c^b - D_1/(R_p^*)^d \quad (3)$$

where $T_c^b = 580$ K is the bulk critical temperature and $R_p^* = R_p - 1.25$ Å is an effective pore radius corresponding to the volume occupied by water. The fitting curve shown in Figure 5 corresponds to the value of the exponent $d = 1.19 \pm 0.04$, which exceeds 1. This means that T_c^h decreases faster than $1/R_p^*$ with decreasing R_p^* . Such behavior should be attributed to the fact that the hysteresis pore critical temperatures correspond to the different values of the well depth U_0 in the pores of different size. The more hydrophilic pore surface is required in smaller pores to achieve the liquid–vapor transition in equilibrium with the saturated bulk water (see Figure 3).

Above the hysteresis pore critical temperature T_c^h , the condensation and evaporation branches of the isotherm $\rho(U_0)$ coincide and the density of water in pore increases in a step-like manner within some rather narrow interval of U_0 (Figure 6). In this interval, several evaporation and condensation transitions of confined water occur in the course of simulations, when temperature is just above T_c^h .¹⁰ We calculated the probability distributions $P(\rho)$ of the density of confined water at $T > T_c^h$ for all pores studied. The distributions $P(\rho)$ for water in pores with radius $R_p = 20$ Å at $T = 500$ K are shown in Figure 7 for several values of U_0 . The pore with $U_0 = -0.99$ kcal/mol contains water vapor during the whole simulation run, and a single peak at low ρ is seen in the distribution $P(\rho)$. At stronger water–surface interactions both vapor and liquid phases can be found in pores during the simulation run and two distant peaks at low and high densities appear. Upon strengthening the water–surface interaction, the liquid peak increases and slightly moves toward higher density whereas the vapor peak decreases and eventually disappears. The occurrence of the liquid–vapor phase transition in some range of U_0 and not at a single value of U_0 indicates that this transition is smeared out due to the intrinsic finite size of the system.³⁹ In the macroscopic limit ($R_p \rightarrow \infty$), the range of U_0 where $P(\rho)$ shows two-peak distribution should vanish.

The two-peak distribution $P(\rho)$ evidences that the system is below the pore critical temperature T_c^p , which is the highest temperature when two phases in a pore can be distinguished.

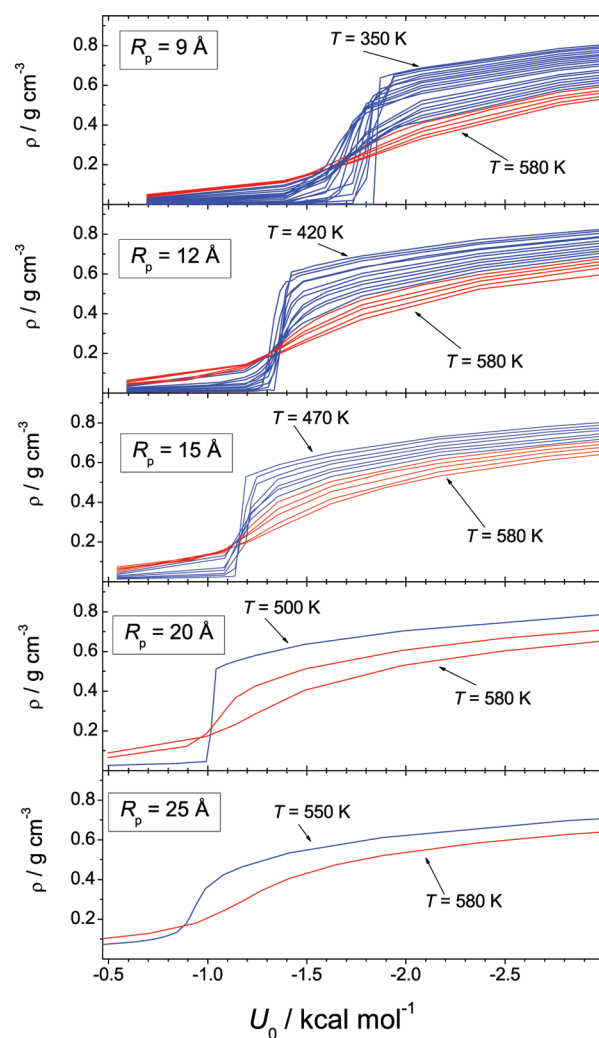


Figure 6. Density of water in pores of various sizes R_p in equilibrium with the saturated bulk as a function of the water–surface interaction U_0 . The isotherms with a single-peak and two-peak density distribution are shown by the red and blue lines, respectively.

Upon heating, two peaks of $P(\rho)$ become wider and approach each other. The evolution of the distribution $P(\rho)$ with temperature is shown for the pore with $R_p = 15$ Å in Figure 8. At $T = 470$ K, the distribution shows pronounced two-peak structure. This structure is still seen at $T = 530$ K, but it disappears at $T = 540$ K. A quite similar picture is seen also for the pores with $R_p = 9$ and 12 Å; the two-peak structure of $P(\rho)$ is still seen at $T = 530$ K. Therefore, $T_c^p = 535 \pm 5$ K for all three pores, which have been studied with a small temperature step. Due to the larger temperature step in the simulations, T_c^p cannot be accurately estimated for the two largest pores with $R_p = 20$ and 25 Å.

The pore critical temperature T_c^p of water in a spherical pore is shown as a function of pore size in Figure 9 together with the values of T_c^p for water in cylindrical and slit pores obtained in our previous studies.³² The values of T_c^p are rather close in pores of different geometry but of comparable size. However, there is a systematic deviation down of the pore critical temperatures of water in cylindrical and spherical pores in comparison with those in slit pores. This difference can be attributed to the rounding of the first-order phase transition and absence of true criticality in cylindrical and spherical pores.^{39,40} The rounding of the phase

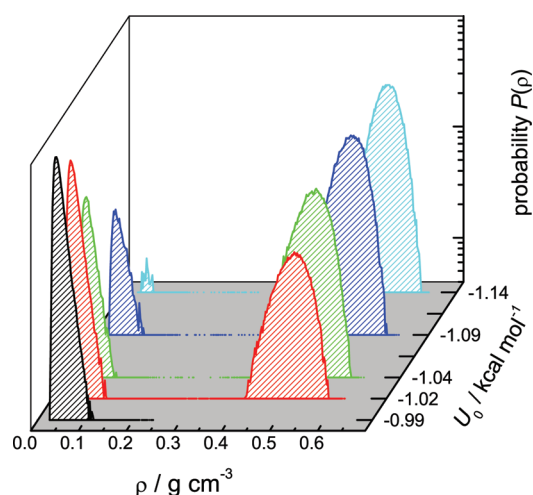


Figure 7. Probability distributions $P(\rho)$ of water density in the pores with radius $R_p = 20$ Å in equilibrium with the saturated bulk at $T = 500$ K for various strengths U_0 of the water–surface interaction.

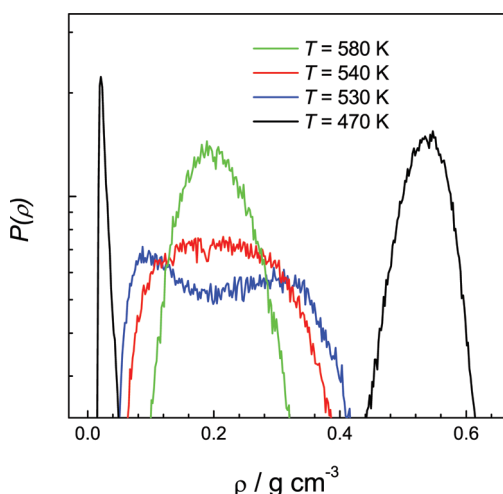


Figure 8. Probability distributions $P(\rho)$ of water density in pores with radius $R_p = 15$ Å in equilibrium with the saturated bulk: $U_0 = -1.165$ kcal/mol at $T = 530$ and 540 K; $U_0 = -1.192$ kcal/mol at $T = 470$ K; $U_0 = -1.220$ kcal/mol at $T = 580$ K.

transition can cause underestimation of the critical temperatures in such pores in simulations.

The shift ΔT_c of the critical temperature in confinement increases with strengthening of the so-called “surface field”, which characterizes the preferential attraction to the surface of one of the components of the system.⁴¹ This shift is minimal for the case of zero surface field, as unavoidable formation of a wetting (drying) layer in the case of nonzero surface field effectively decreases pore size. For the liquid–vapor phase transition, some particular strength of a fluid–surface interaction $U_0 = U_0^c$ provides conditions of the neutral wall corresponding to zero surface field. The deviation of U_0 from U_0^c toward more hydrophobic and more hydrophilic values should cause a decrease of T_c^p due to formation of a drying and wetting layer, respectively. The decrease of T_c^p upon strengthening the fluid–surface interaction and formation of a wetting layer has been reported for water¹⁷ and other fluids.^{16,42} The effect of the

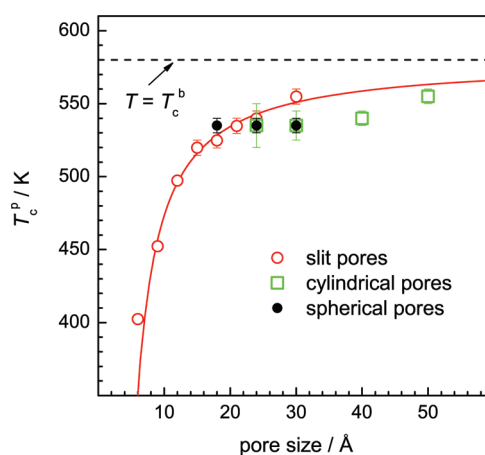


Figure 9. Dependence of the pore critical temperature T_c^p on the pore size (width H for slit pores and diameter $2R_p$ for cylindrical and spherical pores). $U_0 = -0.385$ kcal/mol for slit and cylindrical pores and varies from ca. -1.75 to -1.19 kcal/mol with increasing pore radius from 9 to 15 Å for spherical pores. Error bars for spherical pores correspond to the temperature step used in simulations. The fit of the dependence T_c^p on the pore width H of slit pores to eq 3 is shown by the red line.

drying layer strongly depends on the range of the fluid–surface potential. For long-range fluid–surface interactions, the drying transition occurs at the bulk critical temperature^{43,44} and affects the effective pore size close to the bulk critical temperature only.⁴⁵ This can explain why the values of T_c^p in spherical pores are so close to the value of T_c^b in much more hydrophobic cylindrical pores with $U_0 = -0.385$ kcal/mol (see Figure 9). For short-range fluid–surface interactions (including hard wall), the drying layer can strongly affect the effective pore size and T_c^p nonmonotonously depends on U_0 .^{16,42}

The density of confined water ρ changes gradually upon varying U_0 at $T > T_c^h$. This is the case even below the pore critical temperature T_c^p , as the average density of confined water includes contributions from alternating vapor and liquid states in pores in a course of simulations in the grand canonical ensemble. Due to the continuous change of $\rho(U_0)$, the water–surface interaction U_0^d corresponding to the midpoint of the condensation/evaporation transition of water at the considered temperature can be assigned to the inflection point U_0^d of the isotherm $\rho(U_0)$. The inflection points of $\rho(U_0)$ have been determined by numerical calculation of the derivative $\partial\rho/\partial U_0$ with its subsequent fit by Gaussian. The values U_0^d corresponding to the maximal values of the derivative $\partial\rho/\partial U_0$ are shown in Figure 10 (solid symbols) as a function of temperature for all pores studied. For the pores with $R_p = 12$ and 15 Å, the temperature dependence of U_0^d can be considered as a continuation of the temperature dependence of the stability limit for liquid U_0^{evap} , which decreases weakly with temperature (Figure 10, open symbols). The behavior of U_0^d and U_0^{evap} in larger pores with $R_p = 20$ and 25 Å accords with this conclusion even though there is a smaller number of data points for these pores. The temperature dependence of U_0^d in the smallest pore with $R_p = 9$ Å differs markedly from those in larger pores. Just above T_c^h , U_0^d increases with temperature and only above 460 K it becomes temperature independent, as in other pores. Note that the decrease of the value U_0^d above the pore critical temperature T_c^p is seen for all pores.

Alternatively, the critical value U_0^c corresponding to the condensation/evaporation transition at $T > T_c^h$ can be determined

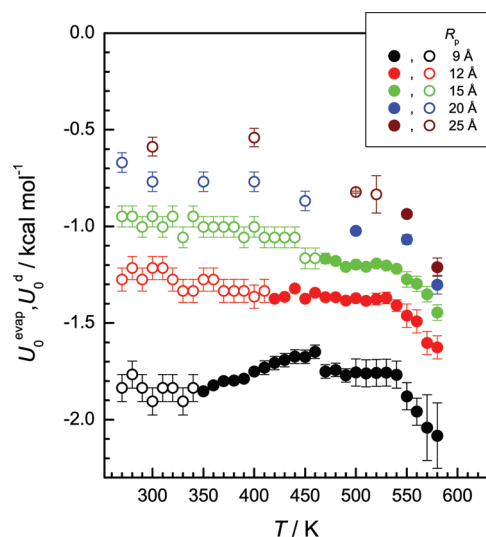


Figure 10. Temperature dependence of the stability limit for the liquid phase (U_0^{evap}) of water in pores of various sizes R_p in equilibrium with the saturated bulk (open circles). Values U_0^d corresponding to the maximum of the derivative $\partial\rho/\partial U_0$ at various temperatures above the hysteresis pore critical temperature, T_c^h , are shown by closed circles. Error bars correspond to the step in U_0 used in simulations.

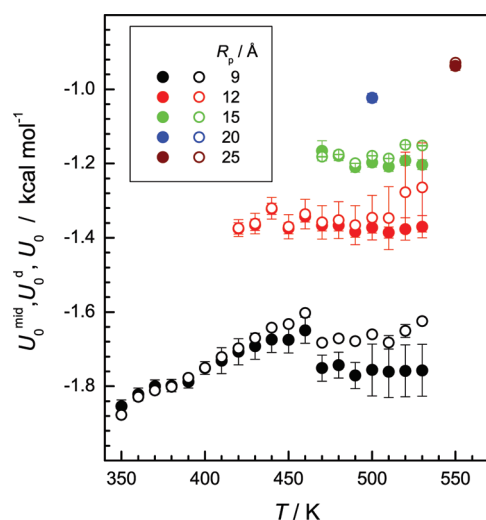


Figure 11. Temperature dependences of U_0^{mid} corresponding to 50% of the probability of a liquid state in a pore (open symbols) and U_0^d corresponding to the inflection point of the isotherm $\rho(U_0)$ (solid symbols). Error bars for U_0^{mid} correspond to errors in the determination of the inflection point of the probability of a liquid state in a pore.

using the probability to observe the liquid (or vapor) water phase in a pore in the course of a simulation run. The probability P_l that water exists in a liquid state can be estimated using the probability distribution $P(\rho)$, which shows a two-peak structure, by its integration for $\rho > \rho_m$, where ρ_m corresponds to the minimum between two peaks of $P(\rho)$ (see ref 10 for more details). At fixed temperature the values of P_l increase upon strengthening the water–pore interaction, and this dependence looks like a sigmoid function (Figure 13 in ref 10). The water–surface interaction potential U_0^{mid} , which corresponds to $P_l = 50\%$, is shown in Figure 11 (open circles) for all pores and temperatures, where

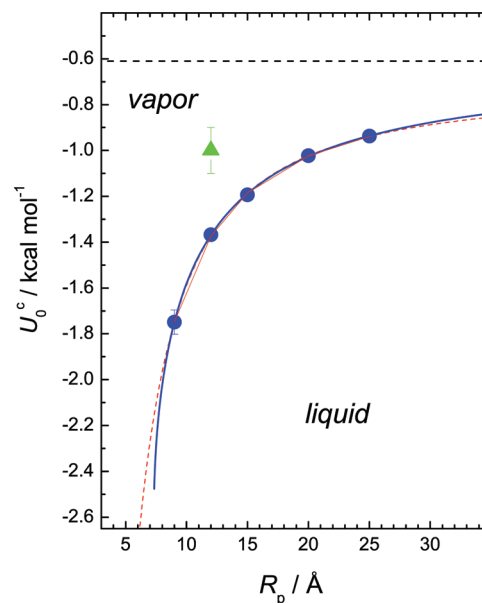


Figure 12. Dependence of the critical water–surface interaction U_0^c on the pore size R_p (blue circles). The fits to eqs 4 and 10 are shown by the red and blue lines, respectively. The critical water–surface interaction for the flat surface $U_0^c(\infty) = -0.61$ kcal/mol obtained from the fit is shown by the horizontal dashed line. The critical interaction U_0^c for water in the cylindrical pore with a radius $R_p = 12$ Å¹³ is shown by the triangle.

the two-peak probability distribution of water density in pores can be seen.

The obtained values of U_0^d and U_0^{mid} are in reasonable agreement (Figure 11). The value U_0^d seems to be more a reliable estimation of U_0^c , as its calculation requires less assumptions than calculations of U_0^{mid} . We cannot detect the temperature dependence of U_0^d between T_c^h and T_c^p within the accuracy of our simulations (excluding the temperature interval between T_c^h and 460 K for the smallest pore). Therefore, we estimated the critical value U_0^c , separating the regimes of capillary condensation and capillary evaporation, as an average value U_0^d in the temperature interval between T_c^h and T_c^p . The dependence of such determined values of U_0^c on the pore radius is shown in Figure 12.

DISCUSSION

In the present paper, we studied the effect of pore size on the condensation/evaporation transition of water in spherical pores in equilibrium with saturated bulk water. The critical water–surface interaction U_0^c , which separates the regimes of capillary condensation and capillary evaporation, was estimated using several procedures and to be found dependent on the size of spherical pores. The values U_0^c were determined in the temperature interval between the hysteresis and the pore critical temperatures and found weakly sensitive to temperature. U_0^c changes from -0.94 to -1.95 kcal/mol when the pore radius R_p decreases from 25 to 9 Å (Figure 12). The dependence $U_0^c(R_p)$ can be satisfactorily fitted to the empirical equation

$$U_0^c(R_p) = U_0^c(\infty) - D_2/(R_p^*)^\beta \quad (4)$$

with $U_0^c(\infty) = (-0.72 \pm 0.03)$ kcal/mol, which is the critical interaction U_0^c in the limit of the macroscopic spherical pore ($R_p \rightarrow \infty$), and $\beta = 1.38 \pm 0.08$. The planar surface with $U_0 = U_0^c(\infty)$ should exhibit neither wetting nor drying transitions.

This agrees reasonably with the simulation studies of the surface transitions of water in large cylindrical pores with $R_p = 25$ Å, where the conditions of the neutral wall have been found at $U_0 \approx -1.0 \pm 0.5$ kcal/mol.⁴⁶

A spherical pore becomes effectively more hydrophobic when the size decreases, i.e., its surface must be more hydrophilic to provide condensation of the saturated bulk vapor. This finding qualitatively agrees with the increase of the contact angle of water droplet on a planar surface with decreasing droplet size seen in simulations.^{47,48} For all pores with $U_0 > U_0^c(\infty)$ only water vapor is a stable phase in equilibrium with the saturated bulk independently of the pore size. For pores with $U_0 < U_0^c(\infty)$, there is some critical pore size R_p^c (see Figure 12), which divides two regimes. In equilibrium with the saturated bulk water, pores with $R_p > R_p^c$ are filled with liquid water whereas pores with $R_p < R_p^c$ contain water vapor. Such surprising behavior is specific for the case of the equilibrium with the saturated bulk water. The situation for the equilibrium with the undersaturated bulk water is opposite: for each degree of saturation, condensation occurs in small pores with sizes below some particular value, defined by the degree of undersaturation.

The size-dependent pore hydrophobicity observed in the present studies can have interesting implications for porous objects immersed in liquid (saturated) water as well as for liquid water at rough surfaces. Small cavities (with $R_p < R_p^c$) of a porous material in liquid water will remain dry even if this material is hydrophilic. This phenomenon can be important also for large macromolecules in liquid water. For example, the value of U_0 for polypeptides varies between -1.8 and -2.4 kcal/mol.⁴⁹ In accordance with the dependence shown in Figure 12, the inner spherical cavities of polypeptides immersed in liquid water can stay dry if their diameters do not exceed ~ 14 Å. The presence of water vapor pockets between a rough surface and liquid water strongly increases the effective hydrophobicity of the surface.⁵⁰ The varying hydrophobicity of small surface areas can affect the contact angle of water at rough surfaces.

It is not clear whether the observed size dependence of the critical value U_0^c is general for all fluids and how it depends on the pore shape. To understand the physical origin of this phenomenon, it is necessary to consider how the conditions of the liquid–vapor equilibrium in the pore in equilibrium with the external bulk fluid can change with decreasing pore size. The difference $\Delta\mu$ of the chemical potentials of a liquid–vapor transition of a fluid in the pore and in the bulk increases with decreasing pore size R_p .^{20,35}

$$\Delta\mu \approx \gamma \cos \theta / R_p \quad (5)$$

where γ is the liquid–vapor surface tension and θ is the contact angle. Such kind of the size dependence of $\Delta\mu$ has been observed in the studies of relatively large pores. The validity of eq 5 worsens with decreasing system size. The presence of the wetting or drying film on the pore surface effectively decreases the size of small pores.^{51,52} Both the surface tension⁵³ and the contact angle⁵⁴ depend on the system size, and these effects can be important in narrow pores. In very narrow pores, the continuous representation of a fluid and, accordingly, determination of γ and $\cos \theta$ are no longer possible.

The critical interaction U_0^c considered in this paper corresponds to the case, when the liquid–vapor transition of confined water occurs at the same value of the chemical potential as in the saturated bulk water, i.e., when $\Delta\mu = 0$. This is possible only

when $\cos \theta = 0$ in eq 5. Therefore, the size dependence of the surface tension γ does not affect directly eq 5 in the particular case of $\Delta\mu = 0$. Additionally, neither wetting nor drying transition occurs at the surface providing $\cos \theta = 0$, and the effect of the wetting or drying layer on the effective pore size can be also excluded. Therefore, we can assume that the dependence of $\cos \theta$ on the system size is the main factor, which causes the dependence of U_0^c on the size of a spherical pore (Figure 12).

The change of the contact angle with decreasing size of a liquid droplet (vapor bubble) on a solid surface has been observed in numerous experiments and simulations.⁵⁴ In particular, simulation studies of the contact angle of water droplet on a planar surface^{47,48} have shown that θ increases with decreasing droplet size. This qualitatively agrees with our results, indicating that the surface becomes effectively more hydrophobic with decreasing system size. The dependence of the contact angle on the system size is usually attributed to the effect of the liquid–vapor–solid line tension.⁵⁴ For the liquid droplet attached to the planar solid wall the contact angle θ depends on the radius r of the liquid–vapor–solid interface⁵⁵

$$\cos \theta = \cos \theta_\infty - \frac{\tau/\gamma}{r} \quad (6)$$

where subscript “ ∞ ” corresponds to a macroscopic droplet and τ is a line tension of the liquid–vapor–solid interface. Thus, the deviation of the contact angle θ from the value θ_∞ increases with decreasing droplet size and the sign of this deviation is determined by the sign of τ . Note that eq 6 is derived assuming constancy of both γ and τ .

For the liquid droplet at the concave spherical surface of radius R_p ⁵⁶

$$\cos \theta = \cos \theta_\infty - \frac{\tau/\gamma}{R_p} \sqrt{(R_p/r)^2 - 1} \quad (7)$$

Thus, the contact angle depends on the pore water density ρ (degree of pore filling) as the length of the liquid–vapor–solid interface r varies from zero to $2\pi R_p$ depending on ρ . It is reasonable to assume that the critical interaction U_0^c corresponds to the case when the “average” contact angle θ_{av} in a pore is equal to 90° . The averaging of θ should be performed among all states exhibiting a liquid–vapor–solid line. To show how the direct liquid–vapor coexistence occurs in a spherical pore, we simulated water in a pore with $R_p = 25$ Å and $U_0 = U_0^c$ at $T = 300$ K in a constant-volume ensemble with water density fixed within the two-phase region. The local density distribution in a slice of 1 Å width at the pore center is shown in Figure 13 for various degrees of pore filling. The blue area corresponds to regions where water density exceeds the value at the midpoint of the bulk liquid–vapor interface. It is difficult to estimate numerically the contact angle due to the density variations near pore surface, complex shape of the liquid–vapor interface, and relatively small number of molecules (especially at low water densities).

The average value S of the square root in the right part of eq 7 does not depend on R_p when it is averaged over the equal probability states with planar liquid–vapor interface. In this approximation, eq 7 can be rewritten as

$$\cos \theta_{av} = \cos \theta_\infty - \frac{S\tau}{\gamma R_p} \quad (8)$$

with $S \approx 0.7$. To use eq 8 for the fit of the dependence $U_0^c(R_p)$ shown in Figure 12, we should relate the water–surface

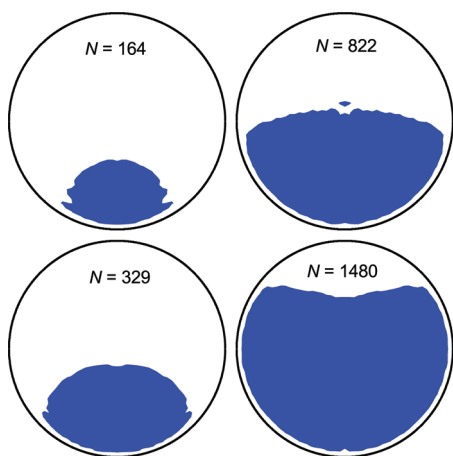


Figure 13. Water density distribution in the spherical pore with $R_p = 25 \text{ \AA}$ at $T = 300 \text{ K}$ and $U_0 = U_0^c$. Blue areas correspond to liquid water. The number N of water molecules in the system is shown in the figure.

interaction strength U_0 to the contact angle θ . Direct simulation studies of the contact angle of water at surfaces with various strengths of the water–surface interaction⁴⁷ have shown that at $T = 300 \text{ K}$ the dependence of the contact angle of water on the well depth U_0 can be well fitted by the linear dependence

$$\theta(U_0) = \theta(0) + KU_0 \quad (9)$$

where $\theta(0)$ is a value of θ in the limit $U_0 \rightarrow 0$. At the liquid–vapor phase transition of confined water in equilibrium with the saturated bulk water, $\cos \theta_{av} = 0$, $U_0 = U_0^c$, and eq 8 can be rewritten as

$$\cos[\theta(0) + KU_0^c]_\infty = \frac{S\tau}{\gamma} \frac{1}{R_p} \quad (10)$$

The dependence $U_0^c(R_p)$ can be perfectly fitted to eq 10 with 3 adjustable parameters: $\theta(0)$, K , and $S\tau/\gamma$. The dependence $\cos \theta(1/R_p)$ obtained from this fit is shown in the upper panel of Figure 14. The slope of this dependence is $S\tau/\gamma = 6.1 \pm 0.2 \text{ \AA}$. Using $S \approx 0.7$, one gets $\tau/\gamma \approx 8.7 \text{ \AA}$. This value is reasonably close to the values τ/γ obtained in the simulation studies of the droplets of SPC/E water on various surfaces,^{47,48} where τ/γ varies from ~ 1 to $\sim 16 \text{ \AA}$ at temperatures between 300 and 400 K.

The dependence of the contact angle θ on the water–surface interaction U_0 obtained from the fit of the dependence $U_0^c(R_p)$ to eq 10 is shown in the lower panel of Figure 14 (red circles). It is strictly linear, as imposed in eq 9. Extrapolation of the linear $\theta(U_0)$ dependence to $U_0 = 0$ yields the maximal value of the contact angle, about 120° near the surface with vanishing water–surface interaction. This is reasonable as the drying transition ($\theta = 180^\circ$) of fluids near the surface exhibiting long-range attraction occurs at the bulk liquid–vapor critical point only.^{43–45} Note also that the largest contact angle of water at a hydrophobic smooth surface of about 120° observed experimentally⁵⁷ agrees well with our result. The dependence $\theta(U_0)$ obtained at $T = 300 \text{ K}$ for SPC/E water⁴⁷ (blue lines in the lower panel of Figure 14) gives higher values of the contact angle with respect to our data, and its extrapolation to $U_0 = 0$ gives an unphysical value above 180° .

Extrapolation of the dependence $\theta(U_0)$ to $\theta = 0$ allows estimation of the interaction potential, which promotes complete wetting. In accordance with the data shown in Figure 14, surfaces

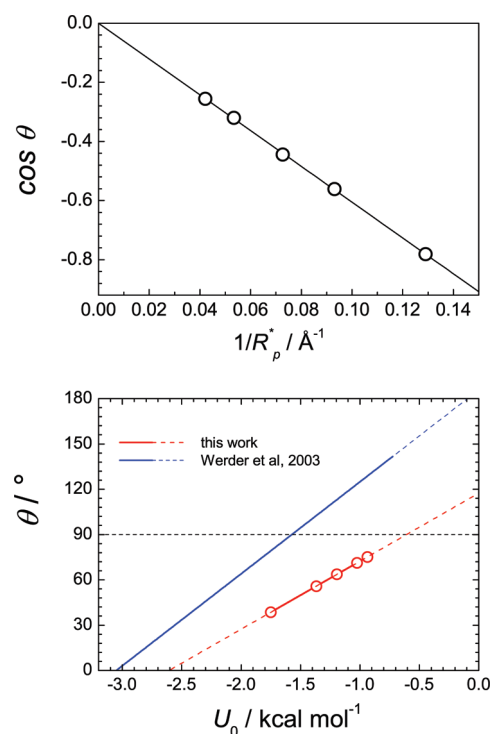


Figure 14. (Top) Dependence of $\cos \theta$ on $1/R_p^*$ obtained from the fit of $U_0^c(R_p)$ to eq 10. (Bottom) Dependence of the contact angle θ on the water–surface interaction U_0 obtained in the present studies and in direct simulations of the contact angle of water at various surfaces.⁴⁷ Solid lines are the linear fits of the dependences $\theta(U_0)$ within the interval of U_0 used in simulations. Extrapolations of these dependences are shown by dashed lines.

with $U_0 < -2.55 \text{ kcal/mol}$ show complete wetting. As we used in the fits the values of U_0^c averaged over some temperature interval it is reasonable to attribute the estimation of the wetting transition at $U_0 \approx -2.55 \text{ kcal/mol}$ to the middle of the temperature interval used in our simulations (about 450 K). This estimation agrees well with the surface phase diagram of water obtained by the simulations of the coexistence curves of the same water model in pores with various U_0 ,⁴⁶ which gives a wetting transition of TIP4P water at $T = 450 \text{ K}$ when $U_0 \approx -2.3 \text{ kcal/mol}$. Note that complete wetting at $T = 300 \text{ K}$ obtained when $U_0 < -3.0 \text{ kcal/mol}$ in ref 47 is remarkably close to the value obtained for TIP4P water at this temperature.¹⁷

The analysis given above shows that the observed dependence of $U_0^c(R_p)$ (Figure 12) can be qualitatively explained by the effect of the line tension on the contact angle using physically reasonable parameters in eq 10. Obviously, an accurate description of this dependence requires direct estimations of the contact angle in pores and its averaging taking into account a complex shape of the liquid–vapor interface in a spherical pore at various degrees of pore filling (see Figure 13). Moreover, the size dependence of τ and γ becomes important with decreasing liquid–vapor interface. For example, the surface tension of a liquid water droplet starts to decrease sharply (by more than 10%) when its diameter is below $\sim 10 \text{ \AA}$.⁵⁸ The limitations in the use of the continuous approximation are probably seen for the smallest pore studied with $R_p = 9 \text{ \AA}$, where U_0^c monotonously increases upon heating from T_c^h to 460 K and abruptly decreases at $T = 470 \text{ K}$ (see Figure 11). Such behavior can be related to the growing

importance of the atomic roughness of interfaces with decreasing system size. The line tension τ is positive for water and the pore becomes more hydrophobic when its size decreases. The negative values of τ have been reported for Lennard–Jones (LJ) fluids.^{59,60} Therefore, for LJ fluids in spherical pores we can expect the dependence $U_0^c(R_p)$ opposite to that shown in Figure 12: U_0^c should increase with decreasing pore size.

The triangle in Figure 12 indicates the critical interaction U_0^c obtained for water in a cylindrical pore with radius $R_p = 12 \text{ \AA}$.¹³ It is essentially larger than the values U_0^c obtained for spherical pores, and we can expect that the effect of the pore size on the critical interaction U_0^c is notably weaker in cylindrical pores. As many real porous materials possess a disordered structure, which includes channels and cavities, the size effect on the critical interaction U_0^c is expected to be significant in such pores. Estimation of the size effect for spherical pores obtained in the present paper (Figure 12) should be considered as the largest possible one for this kind of porous material. In some porous materials the long-range interactions of water molecules with the inner part of a solid material make U_0 dependent on the pore size (see lower panel in Figure 1). This makes the pore surface effectively more hydrophilic with decreasing pore size and partially compensates the effect of the pore size on U_0^c caused by the line tension effect.

The present simulation studies show that the condensation/evaporation transition of confined water being in equilibrium with saturated bulk can be efficiently controlled by varying the water–pore interaction around the critical value U_0^c . The dependence of U_0^c on the pore size causes smearing out of the condensation/evaporation transition in porous materials with the wide pore size distribution. This is an undesirable effect in practical applications, as stronger variations of the water–surface interaction are required in such case to provide complete emptying of the porous material or its complete filling by liquid water. The dependence $U_0^c(R_p)$ shown in Figure 12 allows estimation of the changes ΔU_0 required to provide liquid/vapor transition in the whole pore volume accessible for water. If the porous materials contain pores with $R_p \geq 9 \text{ \AA}$, ΔU_0 is about 1.1 kcal/mol. In the porous material with $R_p \geq 25 \text{ \AA}$, ΔU_0 is about 0.3 kcal/mol. These estimations of ΔU_0 should be considered as an upper limit for the real porous materials.

In the present studies, we considered the case of confined water in equilibrium with the *saturated* bulk water. This case is relevant to technologies, where saturated water vapor is naturally present (for example, in power plants). In many other practical applications, *undersaturated* water vapor from the air is used for condensation in pores. The extension of the diagrams shown in Figures 3 and 12 toward lower humidities of external bulk vapor is required to estimate pore parameters optimal for efficient heat storage in such applications, and this work is in progress now.

AUTHOR INFORMATION

Corresponding Author

*E-mail: ivan.brovchenko@tu-dortmund.de (I.B.); alla.oleynikova@tu-dortmund.de (A.O.).

ACKNOWLEDGMENT

Financial support from the Deutsche Forschungsgemeinschaft is gratefully acknowledged.

REFERENCES

- (1) Liang, L.; Rieke, P.; Liu, J.; Fryxell, G.; Young, J.; Engelhard, M.; Alford, K. *Langmuir* **2000**, *16*, 8016–8023.
- (2) Russell, T. P. *Science* **2002**, *297*, 964–967.
- (3) Liu, Y.; Mu, L.; Liu, B.; Kong, J. *Chem. Eur. J.* **2005**, *11*, 2622–2631.
- (4) Zhang, J.; Han, Y. *Chem. Soc. Rev.* **2010**, *39*, 676–693.
- (5) Deval, J.; Umali, T. A.; Lan, E. H.; Dunn, B.; Ho, C.-M. *J. Micromech. Microeng.* **2004**, *14*, 91–95.
- (6) Ichihashi, T.; Nakano, Y. *Kagaku Kogaku Ronbunshu* **2008**, *34*, 471–476.
- (7) Friebe, A.; Ulbricht, M. *Macromolecules* **2009**, *42*, 1838–1848.
- (8) Tian, B.-S.; Yang, C. *J. Phys. Chem. C* **2009**, *113*, 4925–4931.
- (9) Brovchenko, I.; Oleinikova, A.; Geiger, A.; Schmidt, F. Adsorber and its use in heat accumulators and heat pumps, or refrigerators. Patent DE 102006043672 A1 UPAB 20080523; 2008.
- (10) Brovchenko, I.; Oleinikova, A. *J. Phys. Chem. B* **2010**, *114*, 16494–16502.
- (11) Brovchenko, I.; Paschek, D.; Geiger, A. *J. Chem. Phys.* **2000**, *113*, 5026–5036.
- (12) Brovchenko, I.; Geiger, A.; Paschek, D. *Fluid Phase Equilib.* **2001**, *183*, 331–339.
- (13) Brovchenko, I.; Geiger, A. *J. Mol. Liq.* **2002**, *96*, 195–206.
- (14) Gelb, L.; Gubbins, K.; Radhakrishnan, R.; Sliwinski-Bartkowiak, M. *Rep. Prog. Phys.* **1999**, *62*, 1573–1659.
- (15) Brovchenko, I.; Oleinikova, A. In *Handbook of Theoretical and Computational Nanotechnology*; Rieth, M., Schommers, W., Eds.; American Scientific Publishers: Stevenson Ranch, CA, 2006; Vol. 9, Chapter 3, pp 109–206.
- (16) Zhang, X.; Wang, W. *Phys. Rev. E* **2006**, *74*, 062601.
- (17) Brovchenko, I.; Oleinikova, A. *Interfacial and Confined Water*; Elsevier: Amsterdam, 2008.
- (18) Singh, S. K.; Saha, A. K.; Singh, J. K. *J. Phys. Chem. B* **2010**, *114*, 4283–4292.
- (19) Singh, S. K.; Singh, J. K. *Fluid Phase Equilib.* **2011**, *300*, 182–187.
- (20) Thomson, W. *Philos. Mag.* **1871**, *42*, 448.
- (21) Kresge, C. T.; Leonowicz, M. E.; Vartuli, W. J. R. J. C.; Beck, J. S. *Nature* **1992**, *359*, 710–712.
- (22) Kowalczyk, P.; Jaroniec, M.; Kaneko, K.; Terzyk, A. P.; Gauden, P. A. *Langmuir* **2005**, *21*, 10530–10536.
- (23) Morishige, K.; Yasuki, T. *J. Phys. Chem. C* **2010**, *114*, 10910–10916.
- (24) Calleja, M.; North, A.; Powles, J.; Rickayzen, G. *Mol. Phys.* **1991**, *73*, 973–983.
- (25) Henderson, D.; Sokolowski, S. *Phys. Rev. E* **1995**, *52*, 758–762.
- (26) Keffer, D.; Davis, H. T.; McCormick, A. V. *Adsorption* **1996**, *2*, 9–21.
- (27) Hadjiagapiou, I. A. *Phys. Rev. E* **2002**, *65*, 021605.
- (28) Ravikovitch, P. I.; Neimark, A. V. *Langmuir* **2002**, *18*, 1550–1560.
- (29) Neimark, A. V.; Vishnyakov, A. J. *J. Phys. Chem. B* **2006**, *110*, 9403–9412.
- (30) Jorgensen, W. L.; Chandrasekhar, J.; Madura, J. D.; Impey, R. W.; Klein, M. L. *J. Chem. Phys.* **1983**, *79*, 926–935.
- (31) Allen, M. P.; Tildesley, D. J. *Computer Simulation of Liquids*; Clarendon Press: Oxford, 1987.
- (32) Brovchenko, I.; Geiger, A.; Oleinikova, A. *J. Phys.: Condens. Matter* **2004**, *16*, S5345–S5370.
- (33) Brovchenko, I.; Geiger, A.; Oleinikova, A. *J. Chem. Phys.* **2004**, *120*, 1958–1972.
- (34) Davitt, K.; Rolley, E.; Caupin, F.; Arvengas, A.; Balibar, S. *J. Chem. Phys.* **2010**, *133*, 174507.
- (35) Evans, R.; Marconi, U. M. B.; Tarazona, P. *J. Chem. Phys.* **1986**, *84*, 2376–2399.
- (36) Fisher, M. E.; Nakanishi, H. *J. Chem. Phys.* **1981**, *75*, 5857–5863.
- (37) Morishige, K.; Ito, M. *J. Chem. Phys.* **2002**, *117*, 8036–8041.

- (38) Coasne, B.; Gubbins, K.; Pellenq, R.-M. *Adsorption* **2005**, *11*, 289–294.
- (39) Privman, V.; Fisher, M. *J. Stat. Phys.* **1983**, *33*, 385–417.
- (40) Wilms, D.; Winkler, A.; Virnau, P.; Binder, K. *Phys. Rev. Lett.* **2010**, *105*, 045701.
- (41) Nakanishi, H.; Fisher, M. E. *J. Chem. Phys.* **1983**, *78*, 3279–3293.
- (42) Singh, J. K.; Kwak, S. K. *J. Chem. Phys.* **2007**, *126*, 024702.
- (43) Nightingale, M. P.; Indekeu, J. O. *Phys. Rev. B* **1985**, *32*, 3364–3366.
- (44) Ebner, C.; Saam, W. F. *Phys. Rev. B* **1987**, *35*, 1822–1834.
- (45) Oleinikova, A.; Brovchenko, I.; Geiger, A. *J. Phys.: Condens. Matter* **2005**, *17*, 7845–7866.
- (46) Brovchenko, I.; Oleinikova, A. *J. Phys. Chem. C* **2007**, *111*, 15716–15725.
- (47) Werder, T.; Walther, J.; Jaffe, R.; Halicioglu, T.; Koumoutsakos, P. *J. Phys. Chem. B* **2003**, *107*, 1345–1352.
- (48) Dutta, R.; Khan, S.; Singh, J. K. *Fluid Phase Equilib.* **2011**, *302*, 310–315.
- (49) Oleinikova, A.; Brovchenko, I. *J. Phys. Chem. Lett.* **2011**, *2*, 765–769.
- (50) Hosono, E.; Fujihara, S.; Honma, I.; Zhou, H. *J. Am. Chem. Soc.* **2005**, *127*, 13458–13459.
- (51) Albano, E.; Binder, K.; Heermann, D.; Paul, W. *J. Chem. Phys.* **1989**, *91*, 3700–3706.
- (52) Parry, A.; Evans, R. *J. Phys. A: Math. Gen.* **1992**, *25*, 275.
- (53) Tolman, R. *J. Chem. Phys.* **1949**, *17*, 333–337.
- (54) Amirfazli, A.; Neumann, A. W. *Adv. Colloid Interface Sci.* **2004**, *110*, 121–141.
- (55) Gretz, R. *J. Chem. Phys.* **1966**, *45*, 3160.
- (56) Wolansky, G.; Marmur, A. *Langmuir* **1998**, *14*, 5292–5297.
- (57) Nishino, T.; Meguro, M.; Nakamae, K.; Matsushita, M.; Ueda, Y. *Langmuir* **1999**, *15*, 4321–4323.
- (58) Lu, H. M.; Jiang, Q. *Langmuir* **2005**, *21*, 779–781.
- (59) Ingebrigtsen, T.; Toxvaerd, S. *J. Phys. Chem. C* **2007**, *111*, 8518–8523.
- (60) Weijs, J.; Marchand, A.; Andreotti, B.; Snoeijer, D. L. *J. Phys. Fluids* **2011**, *23*, 022001.